INTERNATIONAL JOURNAL FOR NUMERICAL METHODS IN FLUIDS
Int. J. Numer. Meth. Fluids **28**: 961–981 (1998)

INDIRECT BOUNDARY ELEMENT METHOD FOR SHEAR FLOW OVER PROLATE AND OBLATE HEMISPHEROIDAL PROTUBERANCES ON PLANE WALLS

LISA F. SHATZ*

Research Laboratory of Electronics, Massachusetts Institute of Technology, Cambridge, MA 02139, USA

SUMMARY

The indirect boundary element method was used to study the hydrodynamics of longitudinal shear flow and cross flow with a longitudinal rate of shear over prolate and oblate hemispheroidal protuberances projecting from a plane wall. Analytic techniques such as Fourier analysis, spheroidal co-ordinates, and the method of images were used to make the numerical methods more efficient. A novel method for computing the hydrodynamic torque was used—instead of directly calculating the torque from the weightings of the Green's functions (a method that is only valid when the weightings have physical significance) the hydrodynamic torque was computed indirectly using a Green's function for torque that derived here. As a test of this method, the present scheme was applied to determine the hydrodynamic torque of full spheroids, where exact solutions are known, and excellent results were obtained. Our results for hemispheroids projecting from plane walls were, except for extremely wide oblate hemispheroids, within a factor of two of those of full spheroids. Our results also agreed with those of previous study of oblate hemispheroidal protuberances. © 1998 John Wiley & Sons, Ltd.

KEY WORDS: numerical methods; boundary element method; shear flow; hydrodynamics; spheroids; hair bundles

1. INTRODUCTION

Many phenomena that occur in fluid flow in natural and artificial structures can be modelled as that of shear flow over a protuberance that projects from a plane wall. Examples that occur in artificial structures include flow over a impurity that has been collected on the surface of a collector, and the flow over an irregularity on a rough surface. The micromechanics of the hair bundles that project from the sensory epithelium in the cochlea are studied in the MIT (Massachusetts Institute of Technology) cochlear micromechanics group. Hair bundles exhibit translational and rotational motion. The translational motion of hair bundles at low frequencies is modeled as longitudinal shear flow over hemispheroids projecting from plane walls. The rotational motion at low frequencies is modeled as the superposition of longitudinal shear flow and cross flow with a longitudinal rate of shear.

Studies of longitudinal shear flow over protuberances from plane walls have been carried out previously in 2D [1–3]. Although 2D studies are numerically efficient, they cannot model 3D

---

* Correspondence to: 41 Temple Street, Suffolk University, Boston, MA 02114, USA. Tel.: +1 617 5738234; Fax: +1 617 3675063; E-mail: shatz@kirchoff.ee.suffolk.edu

CCC 0271–2091/98/160961–21$17.50

Received 29 May 1997
Revised 24 November 1997

effects, which can be important in determining the hydrodynamics. There have also been 3D studies of longitudinal shear flow over protuberances, such as that of O'Neill [4], who derived an infinite series solution for flow over a full sphere in contact with a plane wall, and that of Hyman [5] and Price [6], who derived solutions for shear flow over hemispherical bumps. Recently, Pozrikidis [7] derived solutions for oblate hemispheroidal shapes using a direct boundary element method (BEM). The direct BEM method has been used in a number of studies of longitudinal shear flow of an object in the presence of a plane wall [7–10]. The direct method calculates the hydrodynamic properties directly from the weightings of the Green's functions, which represent real, physical quantities.

In this study, the hydrodynamic properties, in particular, the hydrodynamic torques which result from fluid forces on the protuberances, are calculated indirectly. The indirect method is more general—it is valid even when the weightings have no physical significance. To use the indirect method, a Green's function was derived for the hydrodynamic torque from the known Green's functions for hydrodynamic pressure and velocity.

The curvilinear co-ordinate systems, prolate and oblate spheroidal co-ordinates [11,12] were also used to discretize the domain. The use of curvilinear co-ordinates allows for more efficient discretization because regions where the boundaries have high spatial frequencies have the smallest grid spacings. It also allows for more efficient coding with one code describing the full range of prolate hemispheroids and one code for the full range of oblate hemispheroids. To further increase the efficiency of the numerical computation Fourier analysis was used to determine the azimuthal dependence of the weightings, as in a previous study [7]. Therefore, only a one-dimensional discretization was needed. A modified method of images [8,13] was used to represent the boundary conditions along the plane so that discretization along the plane, and the use of artificial boundaries to approximate the behaviour at infinity, were not required.

To check this method, it was applied to full spheroids with no plane present, for which the exact solution is known. The hydrodynamic torque was then computed for full range of prolate and oblate hemispheroidal shapes projecting from plane walls and the results were compared with those for full spheroids [14], and the results for longitudinal shear flow over oblate hemispheroids were compared with those of Pozrikidis [7].

2. PROBLEM FORMULATION

A hemispheroid projecting from a plane wall is shown in Figure 1. Incompressible, Stokes' flow is assumed so that conservation of momentum, and conservation of mass are described respectively by

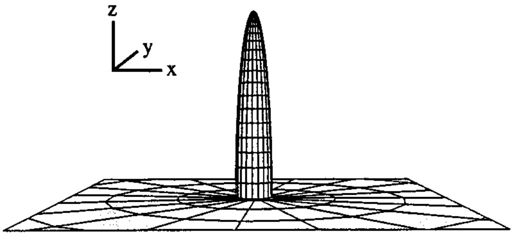

Figure 1. Prolate hemispheroid projecting from a plane wall.

$$\nabla P(\mathbf{r}) = \mu \nabla^2 \mathbf{U}(\mathbf{r}), \tag{1}$$

and

$$\nabla \cdot \mathbf{U}(\mathbf{r}) = 0, \tag{2}$$

where $P(\mathbf{r})$ represents fluid pressure, $\mathbf{U}(\mathbf{r})$, fluid velocity, and μ, fluid viscosity. For longitudinal flow, the boundary conditions along the plane wall and hemispheroid are given by

$$\mathbf{U}(\mathbf{r} = \mathbf{r}') = 0, \tag{3}$$

$$\mathbf{U}(r \to \infty) = -\Omega z \hat{\mathbf{x}}, \tag{4}$$

where $\mathbf{r}'$ represents a vector to a point on the boundaries, Ω represents the angular velocity of the flow, and $\hat{\mathbf{x}}$ represents a unit vector in the x-direction. For cross flow, the boundary conditions are given by

$$\mathbf{U}(\mathbf{r} = \mathbf{r}') = 0, \tag{5}$$

$$\mathbf{U}(r \to \infty) = -\Omega x \hat{\mathbf{z}}. \tag{6}$$

The torque on the hemispheroid is given by

$$\mathbf{T} = \int_S \mathbf{r} \times \mathrm{d}\mathbf{F}(\mathbf{r}), \tag{7}$$

where

$$\mathrm{d}\mathbf{F}(\mathbf{r}) = -P(\mathbf{r})\,\mathrm{d}S + \mu\, \mathrm{d}\mathbf{S} \cdot \nabla \mathbf{U}(\mathbf{r}) + \mu \nabla(\mathrm{d}\mathbf{S} \cdot \mathbf{U}(\mathbf{r})). \tag{8}$$

$\mathbf{r}$ represents a vector to a point on the surface of the hemispheroid, S represents the surface, and $\mathrm{d}\mathbf{S}$ is in the normal direction to the surface. Due to the reflection symmetry about the x–z-plane, the torque has only a y component.

Reference frames can be shifted so that the fluid is stationary at infinity. For this frame of reference, the equations of motion remain the same while the boundary conditions can be expressed as

$$\mathbf{U}(\mathbf{r} = \mathbf{r}') = \Omega z \hat{\mathbf{x}}, \tag{9}$$

$$\mathbf{U}(r \to \infty) = 0, \tag{10}$$

for longitudinal flow, and for cross flow

$$\mathbf{U}(\mathbf{r} = \mathbf{r}') = \Omega x \hat{\mathbf{z}}, \tag{11}$$

$$\mathbf{U}(r \to \infty) = 0, \tag{12}$$

The pressure and the torque are the same for either frame of reference, because for longitudinal flow

$$\mu \nabla^2 (\Omega z \hat{\mathbf{x}}) = 0,$$

and

$$\mathbf{T} = \int_S (\mathbf{r} \times (\mu \nabla(\hat{\mathbf{n}} \cdot \Omega z \hat{\mathbf{x}})) + \mu(\hat{\mathbf{n}} \cdot \nabla)\Omega z \hat{\mathbf{x}}))\,\mathrm{d}S = 0, \tag{13}$$

and cross flow

$$\mu \nabla^2 (\Omega x \hat{\mathbf{z}}) = 0,$$

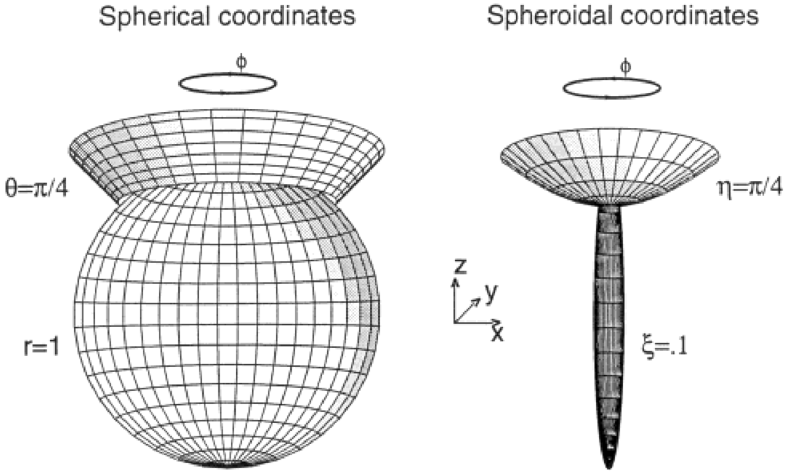

Figure 2. Left: A surface of constant r describes a sphere, and a surface of constant θ describes a half-cone in spherical co-ordinates. Right: A surface of constant ξ describes a spheroid, and a surface of constant η describes a hyperboloid in spheroidal co-ordinates.

and

$$\mathbf{T} = \int_S (\mathbf{r} \times (\mu\nabla(\hat{\mathbf{n}}\cdot\Omega x\hat{\mathbf{z}})) + \mu(\hat{\mathbf{n}}\cdot\nabla)\Omega x\hat{\mathbf{z}}))\,\mathrm{d}S = 0,$$

where $\hat{\mathbf{n}}$ represents a unit normal to the surface. (See Appendix A for the derivation of Equation (13).)

The hydrodynamic quantities will be solved using spheroidal co-ordinates and an indirect BEM method.

3. SPHEROIDAL CO-ORDINATES

We chose to use spheroidal co-ordinates where the hemispheroid and plane wall are co-ordinate surfaces. Spheroidal co-ordinates, represented by ξ, η and ϕ, are similar to spherical co-ordinates, represented by r, θ and ϕ. As with a sphere, a cross-section of a spheroid parallel to the x–y-plane has the shape of a circle; however, a cross-section of a spheroid perpendicular to the x–y-plane has the shape of an ellipse. There are two types of spheroids—prolate and oblate. For prolate spheroids, the heights of the cross-sectional ellipses are larger than the widths; for oblate spheroids, the converse is true. Figure 2 illustrates the similarities and differences between spheroidal and spherical co-ordinates. Spheroidal co-ordinates [11,12] are defined for prolate spheroidal co-ordinates as

$$x = L\sinh\xi\sin\eta\cos\phi, \qquad y = L\sinh\xi\sin\eta\sin\phi, \qquad z = L\cosh\xi\cos\eta, \tag{14}$$

and for oblate spheroidal co-ordinates as

$$x = L\cosh\xi\sin\eta\cos\phi, \qquad y = L\cosh\xi\sin\eta\sin\phi, \qquad z = L\sinh\xi\cos\eta, \tag{15}$$

where L represents the focal length. ξ ranges from 0 to ∞, η ranges from 0 to π, and ϕ ranges from 0 to 2π. An infinitesimal distance is written as

$$(\mathrm{d}s)^2 = (h_1\,\mathrm{d}\xi)^2 + (h_1\,\mathrm{d}\eta)^2 + (h_2\,\mathrm{d}\phi)^2,$$

where h_i are the metric coefficients. For prolate spheroidal co-ordinates, the metric coefficients are expressed as

$$h_1 = L\sqrt{(\sinh^2\xi + \sin^2\eta)},$$

and

$$h_2 = L\sinh\xi\sin\eta.$$

For oblate spheroidal co-ordinates, h_1 and h_2 are given by

$$h_1 = L\sqrt{(\sinh^2\xi + \cos^2\eta)},$$

and

$$h_2 = L\cosh\xi\sin\eta.$$

3.1. Hemispheroid and plane wall

To describe a hemispheroid, η is restricted to range from zero to $\pi/2$. The tip of the hemispheroid is at $\eta = 0$, the base is at $\eta = \pi/2$. Figure 3 illustrates the hemispheroid on a plane wall in rectangular co-ordinates and in spheroidal co-ordinates. In rectangular co-ordinates, the surface of a prolate hemispheroid is described by

$$\frac{x^2+y^2}{(L\sinh\xi_o)^2} + \frac{z^2}{(L\cosh\xi_o)^2} = 1, \quad \text{for } z > 0,$$

and the surface of an oblate hemispheroid,

$$\frac{x^2+y^2}{(L\cosh\xi_o)^2} + \frac{z^2}{(L\sinh\xi_o)^2} = 1, \quad \text{for } z > 0.$$

The surface of the plane wall is described by $z = 0$. In prolate or oblate spheroidal co-ordinates, the surface of the hemispheroid is described by $\xi = \xi_o$ and the surface of the plane wall is described by $\eta = \pi/2$. So it is clear that the hemispheroid and plane wall are co-ordinate surfaces in spheroidal co-ordinates.

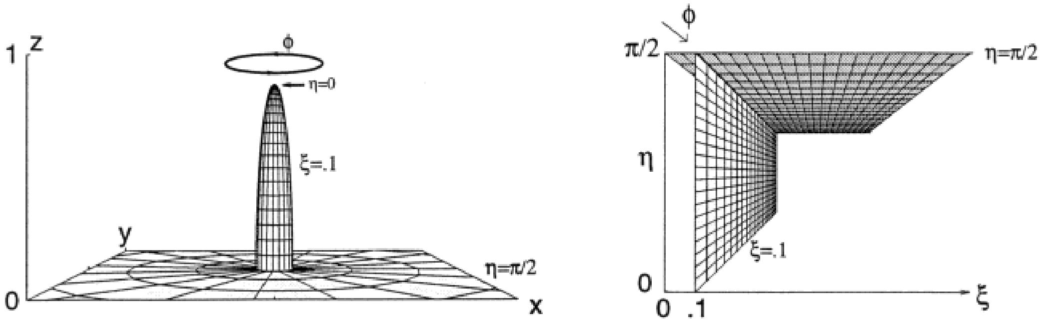

Figure 3. The hemispheroid on a plane wall is defined by a surface of constant ξ and the surface $\eta = \pi/2$. The hemispheroid and plane wall in rectangular co-ordinates (left panel) transform to orthogonal planes in prolate spheroidal co-ordinates (right panel).

4. BOUNDARY ELEMENT METHODS

The BEM is a numerical approximation of the boundary integral or singularity method (BIM), which represents the solutions to a homogeneous linear differential equation with specified boundary conditions as a weighted integral of Green's functions. There are three categories of BEM: indirect, semi-direct and direct [15]. In the indirect BEM, the weightings have no physical significance, but can be integrated to find all the real physical quantities. In the semi-direct BEM, the weightings are not actual physical properties but can be related to physical properties. In the direct method, the weightings represent actual physical properties. Although we could have used the direct method to find the hydrodynamic torque, we chose to calculate the torque indirectly, using a Green's function for torque.

4.1. Green's functions for Stokes' flow

The simplest Green's functions of Equations (1) and (2) are known as stokeslets [16]. $\mathbf{G}_{ux}(\mathbf{r})$, the x component of the velocity stokeslet due to an impulse, can be expressed as

$$\mathbf{G}_{ux}(\mathbf{r}) = \frac{1}{8\pi\mu}\left(\frac{\hat{\mathbf{x}}}{r} + \frac{x^2\hat{\mathbf{x}} + xy\hat{\mathbf{y}} + xz\hat{\mathbf{z}}}{r^3}\right).$$

The other components have similar forms. The pressure stokeslet can be expressed as

$$\mathbf{G}_p(\mathbf{r}) = \frac{1}{4\pi}\left(\frac{x\hat{\mathbf{x}} + y\hat{\mathbf{y}} + z\hat{\mathbf{z}}}{r^3}\right). \tag{16}$$

For Stokes flow in the presence of boundary surfaces, the solution for the ith component of the velocity, where i represents x, y or z, can be expressed as a weighted integral of stokeslets:

$$U_i(\mathbf{r}) = \int_{S'} \mathbf{G}_{ui}(\mathbf{r}, \mathbf{r}')\cdot\mathbf{f}_{\text{fict}}(\mathbf{r}')\,\mathrm{d}S',^1 \tag{17}$$

and the pressure as

$$P(\mathbf{r}) = \int_{S'} \mathbf{G}_p(\mathbf{r}, \mathbf{r}')\cdot\mathbf{f}_{\text{fict}}(\mathbf{r}')\,\mathrm{d}S'. \tag{18}$$

$\mathbf{f}_{\text{fict}}(\mathbf{r}')$ represents the weightings of the impulses along the surface. In contrast to the direct method, $\mathbf{f}_{\text{fict}}(\mathbf{r}')$, does not represent a real point force and has no physical significance. From Equations (7) and (8), the torque exerted by the ith component of an impulse on a surface S surrounding the impulse can be expressed as

$$\mathbf{G}_{Ti}(\mathbf{r}') = \int_S \bar{\mathbf{G}}_{Ti}(\mathbf{r}', \mathbf{r})\,\mathrm{d}S, \tag{19}$$

where

$$\bar{\mathbf{G}}_{Ti}(\mathbf{r}) = \mathbf{r}\times(\hat{\mathbf{n}}G_{pi}(\mathbf{r}) + \mu\nabla(\hat{\mathbf{n}}\cdot\mathbf{G}_{ui}(\mathbf{r})) + \mu(\hat{\mathbf{n}}\cdot\nabla)\mathbf{G}_{ui}(\mathbf{r})), \tag{20}$$

and can be considered a Green's function for torque per unit area. The Green's function given in Equations (19) and (20) can be considered as the torque stokeslet; therefore the ith component of torque can be expressed as

---

[1] This is true because the ith component of a velocity stokeslet due to an in impulse in the jth direction is equal to the jth component of a velocity stokeslet due to an in impulse in the ith direction.

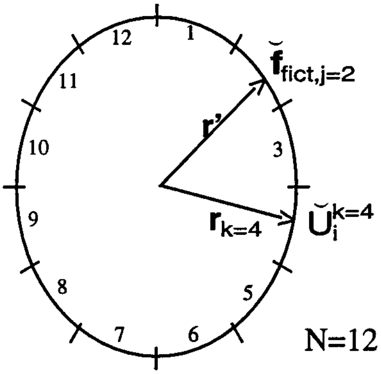

Figure 4. In the BEM, the surface is broken into N elements, and the weightings of the impulses are assumed to be constant in an element. The ith component of velocity of the kth element is given by $\check{U}_i^k = \Sigma_{j=1}^N \int_{\mathrm{d}S'} \mathbf{G}_{ui}(\mathbf{r}_k, \mathbf{r}')\cdot\check{\mathbf{f}}_{\text{fict},j}\,\mathrm{d}S'$.

$$T_i = \int_{S'} \mathbf{G}_{Ti}(\mathbf{r}')\cdot\mathbf{f}_{\text{fict}}(\mathbf{r}')\,\mathrm{d}S'.$$

4.2. Boundary element methods

For most problems, $\mathbf{f}_{\text{fict}}$ cannot be obtained by analytic techniques, and a numerical approximation of the boundary integral method, the BEM, is used to obtain an approximation of $\mathbf{f}_{\text{fict}}$ [17]. With the BEM, the surface boundaries are broken into N elements with an approximation of $\mathbf{f}_{\text{fict}}$ in each element. There are many ways to approximate the continuous BIM with a discrete representation. A constant approximation for $\mathbf{f}_{\text{fict}}$ is used here, so that the integrals of Equations (17) and (18) become sums, i.e.

$$U_i(\mathbf{r}) \approx \sum_{j=1}^{N} \int_{\mathrm{d}S'_j} \mathbf{G}_{ui}(\mathbf{r}, \mathbf{r}')\cdot\check{\mathbf{f}}_{\text{fict},j}\,\mathrm{d}S'_j,$$

$$P(\mathbf{r}) \approx \sum_{j=1}^{N} \int_{\mathrm{d}S'_j} \mathbf{G}_p(\mathbf{r}, \mathbf{r}')\cdot\check{\mathbf{f}}_{\text{fict},j}\,\mathrm{d}S'_j.$$

$\check{\mathbf{f}}_{\text{fict}}$ is the piecewise constant approximation of $\mathbf{f}_{\text{fict}}$. A collocation method is used to obtain $\check{\mathbf{f}}_{\text{fict}}$. The surface is broken into N elements and $U_i(\mathbf{r})$ is approximated as $\check{U}_i^k$, a piecewise constant function, with $\check{U}_i^k = U_i(\mathbf{r}_k)$, the velocity at the midpoint of the kth element. $\check{U}_i^k$ is set to the known boundary conditions $U_{\text{surf},i}(\mathbf{r}_k)$, so that

$$U_{\text{surf},i}(\mathbf{r}_k) = \check{U}_i^k = \sum_{j=1}^{N} \int_{\mathrm{d}S'_j} \mathbf{G}_{ui}(\mathbf{r}_k, \mathbf{r}')\cdot\check{\mathbf{f}}_{\text{fict},j}\,\mathrm{d}S'_j. \tag{21}$$

The midpoint of each element is known as the collocation point. $\check{\mathbf{f}}_{\text{fict}}$ is found by solving Equation (21), for each element, for each component of the velocity (Figure 4).

4.3. Non-integrable singularities in the pressure and torque stokeslets

The pressure and torque stokeslets have non-integrable singularities on the boundary surface. However, the torque on the body can still be calculated exactly, despite the non-integrable singularity. This is because the integration over S need not be over the surface of the body—any surface that encloses the stokeslets will suffice because the torque induced by the fluid on a closed surface is zero, i.e.

$$\mathbf{T}=\int_S \mathbf{r}\times(P\mathbf{n}-\bar{\tau}\mathbf{n})=\int_V \mathbf{r}\times(\nabla P(\mathbf{r})-\mu\nabla^2 U(\mathbf{r}))\,\mathrm{d}V=0,$$

where $\bar{\tau}$ is a tensor that represents the fluid shear. Appendix B contains a derivation of this result. The choice of surrounding surface for a hemispheroid is described in Section 7.4.

4.4. Simplifications for structures with rotational symmetry about the z-axis, with motions only in the x–z-plane

Using Fourier analysis, we can derive the ϕ' dependence of $\mathbf{f}_{\text{fict}}(\mathbf{r}')$ for the spheroidal structures that are considered in this paper. It can be shown [18] that for structures that are symmetric about the z-axis, and with motions only in the x–z-plane, the hydrodynamic pressure and velocity can be expressed as

$$P(\xi,\eta,\phi)=f_1(\xi,\eta)\cos\phi, \tag{22}$$

$$U_x(\xi,\eta,\phi)=f_2(\xi,\eta)\cos^2\phi+f_3(\xi,\eta), \tag{23}$$

$$U_y(\xi,\eta,\phi)=f_4(\xi,\eta)\cos\phi\sin\phi, \tag{24}$$

$$U_z(\xi,\eta,\phi)=f_5(\xi,\eta)\cos\phi, \tag{25}$$

where $f_1, f_2, \ldots, f_5$ are general functions that together, with the indicated ϕ dependencies, solve Equations (1) and (2). The known ϕ dependence of the pressure is used here to derive the ϕ' dependence of $\mathbf{f}_{\text{fict}}$. This analysis requires only boundary surfaces of spheroids, so that $\mathbf{f}_{\text{fict}}$ depends only on η' and ϕ' and is independent of ξ'. The results are checked by investigating whether the resulting velocities induced by the stokeslets have the correct ϕ dependence.

The steps of the method used to obtain the ϕ' dependence are summarized as follows:
Step 1: Represent $\mathbf{f}_{\text{fict}}(\mathbf{r}')$ as a Fourier series in ϕ',

$$\mathbf{f}_{\text{fict}}(\eta',\phi')=\sum_{j=0}^{\infty}((\tilde{a}_{xj}(\eta')\cos(j\phi')+\tilde{b}_{xj}(\eta')\sin(j\phi'))\hat{\mathbf{x}}+(\tilde{a}_{yj}(\eta')\cos(j\phi')+\tilde{b}_{yj}(\eta')\sin(j\phi'))\hat{\mathbf{y}}$$
$$+(\tilde{a}_{zj}(\eta')\cos(j\phi')+\tilde{b}_{zj}(\eta')\sin(j\phi'))\hat{\mathbf{z}}). \tag{26}$$

Step 2: Express $G_p(\mathbf{r},\mathbf{r}')$ in spheroidal co-ordinates.
Step 3: Calculate $P(\mathbf{r})=\int \mathbf{G}_p(\mathbf{r},\mathbf{r}')\cdot\mathbf{f}_{\text{fict}}(\eta',\phi')\,\mathrm{d}\eta'\,\mathrm{d}\phi$. Let $\phi''=\phi'+\phi$, and perform the integration in ϕ'' instead of ϕ'. This shift simplifies the integration, but does not affect it because the integral is over a full period. The terms that are odd functions of ϕ'' integrate to zero.
Step 4: See which terms of the Fourier series of $\mathbf{f}_{\text{fict}}(\mathbf{r}')$ give the pressure terms with $\cos\phi$ dependence.
Step 5: The result is

$$f_{\text{fict},x}(\eta',\phi')=a_{x0}(\eta')+a_{x2}(\eta')\cos^2\phi', \tag{27}$$

$$f_{\text{fict},y}(\eta',\phi')=a_{x2}(\eta')\sin\phi'\cos\phi', \tag{28}$$

$$f_{\text{fict},z}(\eta',\phi')=a_{z1}(\eta')\cos\phi', \tag{29}$$

where $a_{x0}(\eta')=\tilde{a}_{x0}(\eta')-\tilde{a}_{x2}(\eta')$, $a_{x2}(\eta')=2\tilde{a}_{x2}(\eta')$, and $a_{z1}(\eta')=\tilde{a}_{z1}(\eta')$. A similar method was used by Pozrikidis [7], who performed the analysis in cylindrical co-ordinates. Appendix C contains a more detailed derivation.

5. ANALYSIS FOR FULL SPHEROIDS

The results of the present method applied to a stationary full spheroid in longitudinal shear flow are described in this section. The numerics will be further simplified by using symmetry to predict the stokeslet weightings in the lower half of the spheroid. There are known exact solutions (see Appendix D), therefore, we can check our results. This exercise also serves as a partial check of this method applied to a hemispheroid on a plane wall because there is much overlap in the numerical code used to solve the two problems.

5.1. Boundary conditions

For longitudinal shear flow, let the fluid velocity far from the spheroid be represented by $-\Omega z\hat{\mathbf{x}}$. If reference frames are shifted to be such that the fluid is stationary at infinity, the fluid velocity along the surface of the spheroid, in the new reference frame, is given by

$$\mathbf{U}(\xi = \xi_o, \eta, \phi) = \Omega z\hat{\mathbf{x}}.$$

Exact solutions to the Stokes equation with these boundary conditions, as well as those for cross flow, are found in Appendix D.

5.2. Symmetry

Because the spheroid and boundary conditions are symmetric about the equatorial plane, only a half contour of constant ϕ above the equator needs to be discretized, provided an image stokeslet is added or subtracted to the stokeslet. The **x**- and **y**-components of stokeslets due to impulses in $\hat{\mathbf{x}}$ are symmetric about the equatorial plane, as is the **z**-component of stokeslets due to impulses in $\hat{\mathbf{z}}$. The other stokeslets are antisymmetric. Since the boundary conditions are symmetric in $\hat{\mathbf{z}}$ but are antisymmetric in $\hat{\mathbf{x}}$, the sign of the image stokeslets in $\hat{\mathbf{x}}$ are negative.

5.3. The numerical method

The Green's functions are integrated numerically with respect to η' using an iterative trapezoidal rule with a user specified relative accuracy set by a parameter ϵ, which is defined as

$$\epsilon = \frac{|a_{\text{new}} - a_{\text{old}}|}{a_{\text{new}}},$$

where a_{new} is the latest estimate and a_{old} is the previous estimate. The matrix is inverted using Mathematica's inverse subroutine [19], which inverts this type of matrix by Gaussian elimination.

5.4. The torque calculation

The calculation of the torque is somewhat more complicated than that of velocity and pressure because an additional integration over the surface is required. Using Equations (19) and (20), the torque, which, for the structures considered here, is completely in $\hat{\mathbf{y}}$, can be expressed as

$$T_y \approx \int_S \mathrm{d}S \sum_{j=1}^{N} \int_{\mathrm{d}S'_j} \bar{\mathbf{G}}_{ti}(\mathbf{r}, \mathbf{r}') \cdot \check{\mathbf{f}}_{\text{fict},j} \, \mathrm{d}S'_j.$$

The torque can be found by first analytically integrating $\bar{\mathbf{G}}_{ti}(\mathbf{r}, \mathbf{r}')$ over ϕ' and ϕ, numerically integrating over $\mathrm{d}\eta'$, summing the dot product of the result and the fictitious sources, integrating over $\mathrm{d}\eta$, and then summing the result, giving

$$
\begin{aligned}
T_y &\approx \sum_{k=1}^{N} \int_{\pi(k-1)/N}^{\pi k/N} \mathrm{d}\eta\, h_1(\eta, \xi) h_2(\eta, \xi) \\
&\quad \times \sum_{j=1}^{N} \int_{\pi(j-1)/N}^{\pi j/N} \mathrm{d}\eta'\, h_1(\eta', \xi') h_2(\eta', \xi') \int_{\phi} \mathrm{d}\phi \int_{\phi'} \mathrm{d}\phi'\, \bar{\mathbf{G}}_{ti}(\mathbf{r}_k, \mathbf{r}') \cdot \check{\mathbf{f}}_{\mathrm{fict},j} \\
&= 2 \sum_{k=1}^{N/2} \int_{\pi(k-1)/2N}^{\pi k/2N} \mathrm{d}\eta\, h_1(\eta, \xi) h_2(\eta, \xi) \hat{g}_{1,k},
\end{aligned}
$$

with

$$
\hat{g}_{1,k} = \sum_{j=1}^{N/2} \int_{\pi(j-1)/2N}^{\pi j/2N} \mathrm{d}\eta'\, h_1(\eta', \xi') h_2(\eta', \xi') \int_{\phi} \mathrm{d}\phi \int_{\phi'} \mathrm{d}\phi' (\bar{\mathbf{G}}_{ti}(\mathbf{r}_k, \mathbf{r}') \pm \bar{\mathbf{G}}_{ti}(\mathbf{r}_k, \mathbf{r}'_{\mathrm{image}})) \cdot \check{\mathbf{f}}_{\mathrm{fict},j},
$$

where $\hat{g}_{1,k}$ is a piecewise constant function. The + is used for the stokeslets due to impulses in $\hat{\mathbf{z}}$ and the − for stokeslets due to impulses in $\hat{\mathbf{x}}$. To obtain a better approximation to the torque, a fitted polynomial approximation to $\hat{g}_{1,k}$ is used, i.e.

$$
T_y \approx 2 \int_0^{\pi/2} h_1(\eta, \xi) h_2(\eta, \xi) g_1(\eta)\, \mathrm{d}\eta,
$$

where $g_1(\eta)$ is the fitted polynomial to $\hat{g}_{1,k}$.

6. RESULTS FOR FULL SPHEROIDS

To understand the sources of error in our torque calculation, the normalized torque $T_y/(\mu\Omega)$ was computed for different shapes (Figure 5) and the results compared with those of the exact solution (Table I). We also verified our code by checking that the torque on different surfaces surrounding the spheroid is the same—this implies that the torque induced by the fluid is zero and that Stokes equation is satisfied. The spheroid is denoted by a surface of constant ξ_o, and the different surrounding surfaces are denoted by ξ.

Three features are evident: the error is small (maximum error is 1.6% for $N = 4$); the error decreases with the distance between the surrounding surface and the spheroidal surface; and the error decreases (although not monotonically) with increasing N. The decrease with N is to be expected—the piecewise constant approximation improves with increasing N; the fact that the decrease is not monotonic may be due to the additional source of error in the torque calculation coming from the polynomial fit approximation. The decrease in error with distance can be understood—as the distance from the surface of the spheroid increases, the distance from the non-integrable singularities increases, and the numerical integration can be performed more accurately.

7. HEMISPHEROID PROJECTING FROM A PLANE WALL

7.1. *Boundary condition along plane wall*

The problem of a hemispheroid projecting from a plane wall is similar in many ways to the problem of a full spheroid. It has the same axial symmetry, and the motion of the body is solely in the x–z-plane. Therefore, the ϕ dependence of the stokeslet weightings is known. The main difference in applying the present method to a hemispheroid projecting from a plane wall is satisfying the boundary condition along the infinite plane wall. We could discretize a contour along the wall in addition to the contour along the hemispheroid, and find the stokeslet weightings that would satisfy the boundary conditions, but the computational domain must be finite. Therefore, artificial boundaries would have to be introduced in the fluid at some distance away from the hemispheroid, but the use of artificial boundaries would introduce errors. An alternate method, the method used here, is to use a Green's function that has the correct boundary conditions along the plane wall.

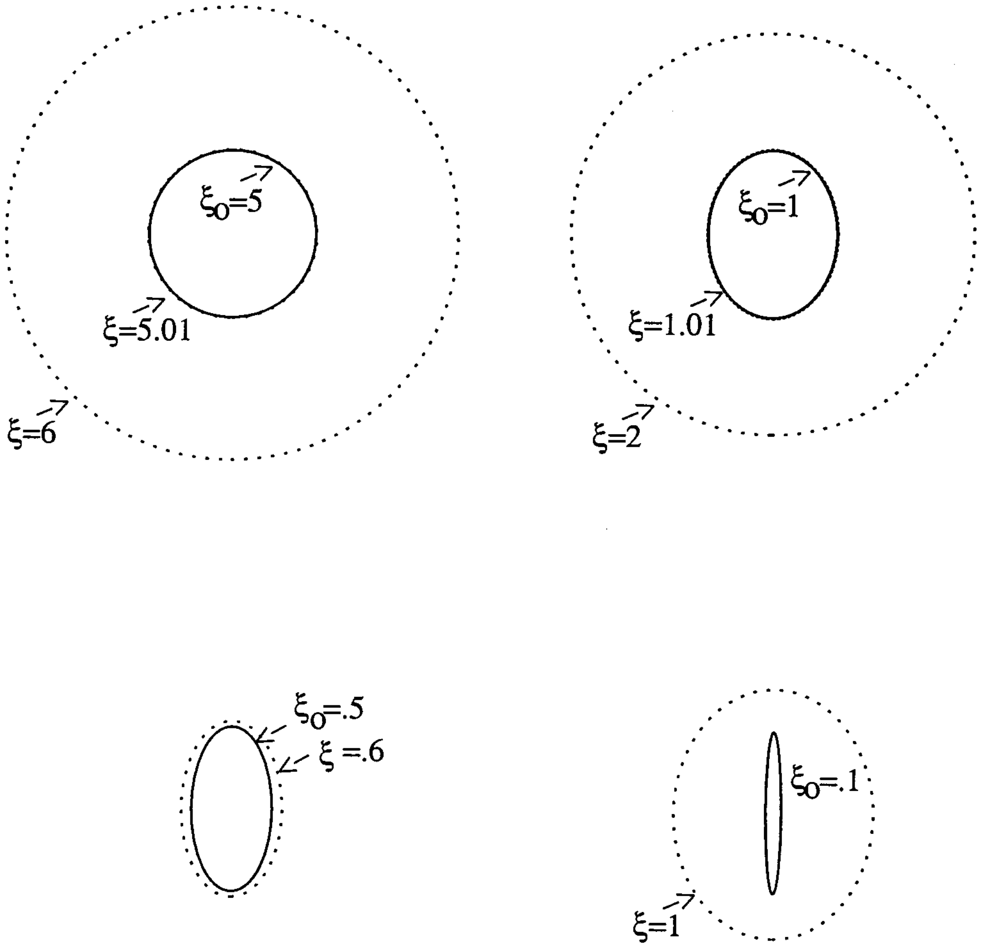

Figure 5. The spheroids for which the torque was calculated (solid lines) along with the enclosing surfaces (dotted lines) used in the calculation.

Table I. Results for the normalized torque, $T_{ny} = T_y/(\mu\Omega)$, calculated for spheroids with different ξ_o

Analytic	Numeric	% error	N	ξ	ξ_o
−12.57	−12.77	1.6	4	5.01	5
−12.57	−12.52	0.4	8	5.01	5
−12.57	−12.42	1.2	16	5.01	5
−12.57	−12.56	0.1	32	5.01	5
−12.57	−12.55	0.2	64	5.01	5
−12.57	−12.56	0.1	8	6.00	5
−10.18	−10.11	0.7	8	1.01	1
−10.18	−10.17	0.1	8	2.00	1
−7.18	−7.15	0.4	8	0.60	0.50
−7.18	−7.18	0.0	16	0.60	0.50
−7.18	−7.18	0.0	32	0.60	0.50
−3.33	−3.33	0.0	8	1.00	0.1

The torque is calculated on different surfaces surrounding the spheroid (the surfaces are denoted by ξ), for different discretizations (N).

7.2. The Green's function for a stokeslet in the presence of a plane wall

The jth component of the Green's function for velocity due to a stokeslet in the kth direction in the presence of a plane wall can be expressed as [13]

$$G^k_{u,\mathrm{wall},j}(\mathbf{r}, \mathbf{r}') = G^k_{u,j}(\mathbf{r}, \mathbf{r}') - G^k_{u,j}(\mathbf{r}, \mathbf{r}'_{\mathrm{image}}) + G^k_{uw,j}(\mathbf{r}, \mathbf{r}'_{\mathrm{image}}),$$

where $G^k_{u,j}(\mathbf{r})$ is the jth component of velocity due to a stokeslet in the kth direction with no wall present, $r'_{\mathrm{image}} = x'\hat{\mathbf{x}} + y'\hat{\mathbf{y}} - z'\hat{\mathbf{z}}$, and $G^k_{uw,j}(\mathbf{r}, \mathbf{r}'_{\mathrm{image}})$ satisfies Stokes equation, and has the necessary velocity along the wall to ensure that $G^k_{u,\mathrm{wall},j}(\mathbf{r}, \mathbf{r}')$ equals zero along the wall. $G^k_{uw,j}(\mathbf{r}, \mathbf{r}'_{\mathrm{image}})$ can be expressed as

$$G^k_{uw,j}(\mathbf{r}, \mathbf{r}'_{\mathrm{image}}) = \frac{1}{4\pi\mu} z'(\delta_{k\alpha}\delta_{\alpha l} - \delta_{k3}\delta_{3l}) \times \frac{\partial}{\partial(x_l - x'_{\mathrm{image}})}\left[\frac{z'(x_j - x'_{j,\mathrm{image}})}{|\mathbf{r} - \mathbf{r}'_{\mathrm{image}}|^3} - \left(\frac{\delta_{j3}}{|\mathbf{r} - \mathbf{r}'_{\mathrm{image}}|} + \frac{(x_j - x'_{j,\mathrm{image}})(z + z')}{|\mathbf{r} - \mathbf{r}'_{\mathrm{image}}|^3}\right)\right],$$

where δ_{ij} represents the Kronecker delta function. The Green's function for pressure due to a stokeslet in the kth direction in the presence of a wall can be expressed as

$$G^k_{p,\mathrm{wall}}(\mathbf{r}, \mathbf{r}') = G^k_p(\mathbf{r}, \mathbf{r}') - G^k_p(\mathbf{r}, \mathbf{r}'_{\mathrm{image}}) + G^k_{pw}(\mathbf{r}, \mathbf{r}'_{\mathrm{image}}),$$

where $G^k_p(\mathbf{r})$ is the pressure due to a stokeslet in the kth direction with no wall present, and $G^k_{pw}(\mathbf{r}, \mathbf{r}'_{\mathrm{image}})$ accounts for the presence of the wall,

$$G^k_{pw}(\mathbf{r}, \mathbf{r}'_{\mathrm{image}}) = \frac{-z'}{2\pi}(\delta_{k\alpha}\delta_{\alpha l} - \delta_{k3}\delta_{3l})\frac{\partial}{\partial(x_l - x'_{l,\mathrm{image}})}\frac{z + z'}{|\mathbf{r} - \mathbf{r}'_{\mathrm{image}}|^3}.$$

These Green's functions are mathematically equivalent to a Stokes doublet and source doublet in the image plane [13].

7.3. Method for hemispheroid projecting from a plane wall

For the full spheroid, the hydrodynamics were represented as a weighted integral of stokeslets. For the hemispheroid projecting from a wall, the hydrodynamics will be represented as a weighted integral of the vector sum of a stokeslet, an image stokeslet, a Stokes doublet and a source doublet.

As mentioned above, the ϕ dependence of the weightings are already known. To obtain the source weightings in η, a similar procedure to the one outlined for the full spheroid is used, except that we have additional sources to the stokeslet and image stokeslet.

7.4. The torque calculation for a hemispheroid projecting from a plane wall

Because of the presence of the infinite plane wall, a surface surrounding the sources cannot be used to calculate the torque. However, the torque can be calculated by integrating over the surface indicated by the dashed lines in Figure 6, because the torque induced by the fluid on the surface described by the hemispheroid and the dashed lines is equal to zero. Therefore, the torque along the dashed lines is equal to the negative of the torque induced by the fluid on the hemispheroid.

7.5. Check that the torque on a surface that encloses only fluid is zero

If Stokes equation is satisfied, then the torque on a surface that encloses only fluid must be zero. To test that this was so, we performed the following calculation. We computed the torque along three different surfaces indicated by the dashed curves in Figure 7. The indicated surfaces, along with the surface of the hemispheroid, encloses only fluid. Therefore the total torque computed along the surfaces is zero. This implies that the torque calculated for the surfaces indicated by the dashed curves must be equal to the negative of the torque calculated along the surface of the hemispheroid. We checked that the torque computed for several different surfaces in the fluid remains the same. Figure 7 illustrates the enclosing surfaces as well as the torques for a nearly hemispherical shape. We see that the difference in torque is $< 3\%$. The errors derive from the discretization and the polynomial fit used in the torque calculation (see Section 5.4).

Table II illustrates the results for Figure 7 as well as the results for a thin, prolate hemispheroid, $\xi_o = 0.5$. For the thin, prolate hemispheroid, the differences were $< 0.1\%$.

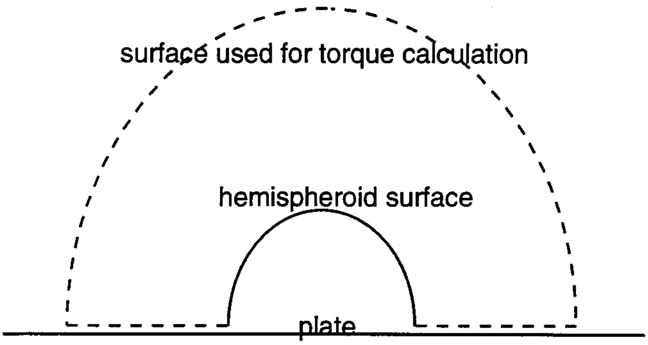

Figure 6. The torque on the surface indicated by the dashed lines is equal to the negative of the torque on the hemispheroid. The solid line indicates the hemispheroid.

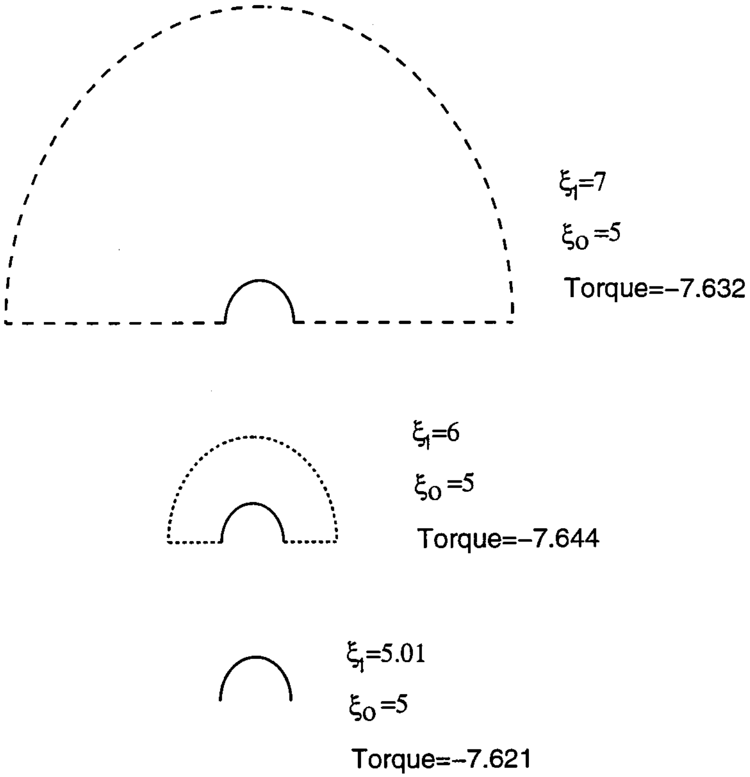

Figure 7. The dashed lines indicate $\xi = \xi_1$, the surfaces for which the torque was computed. The solid line indicates the surface of the hemispheroid, $\xi = \xi_o = 5$. The sum of the torques computed for surfaces indicated by solid and dashed lines is zero since the surfaces enclose fluid. Three different surfaces in the fluid were chosen. The torque for the three dashed surfaces must be the same and must be equal to the negative of the torque for the hemispheroidal surface.

Table II. The torque computed along surfaces for different hemispheroid shapes

Torque	N_1	N_2	ξ	ξ_o
−7.621	8	8	5.01	5
−7.644	8	100	6.00	5
−7.626	8	100	7.00	5
−7.632	8	200	7.00	5
−4.050	16	8	0.501	0.5
−4.053	16	25	0.60	0.5
−4.053	16	50	0.70	0.5

N_1 denotes the number of elements along the hemispheroidal contour. N_2 denotes the number of elements used along the wall. A polynomial fit of the torque/η was used to perform the integration along the contours.

Table III.

ξ_o	Our results	Other results
5	7.67	7.70
0.55	15.40	15.40
0.2	44.0	43.3
0.1	100	94.2

8. COMPARISON OF RESULTS FOR OBLATE HEMISPHEROIDS WITH THOSE OF A PREVIOUS STUDY FOR LONGITUDINAL SHEAR

Table III shows a comparison of our results with those of a previous study [7], for oblate hemispheroids for longitudinal shear. The percentage difference is very small ($<0.2\%$) for narrower oblate hemispheroids and is largest (6%) for the extremely wide oblate hemispheroid. The increase in error may be due to the effect of the artificial boundaries used in the other method, which would be larger for wider hemispheroids.

9. RESULTS FOR THE FULL RANGE OF SHAPES FOR FULL SPHEROIDS AND HEMISPHEROIDS

9.1. Hydrodynamic torque

The hydrodynamic torque as a function of shape is illustrated in Figure 8. The parameter ξ_o defines the shape. As $\xi_o \to \infty$, the shape of prolate and oblate spheroids approaches spherical. As $\xi_o \to 0$, these shapes become the most eccentric, with the shape of a prolate spheroid approaching that of a line segment, and the shape of an oblate spheroid approaching that of a thin, wide disk. The hydrodynamic torque for hemispheroids with longitudinal shear (which results from translational motion) is illustrated in the left panel of Figure 8. The torque is normalized by the cube of the height of the hemispheroid. With this normalization, the torque varies by less than an order of magnitude for the full range of shapes. For translational motion, for thin prolate hemispheroids, the torque for the hemispheroid projecting from a

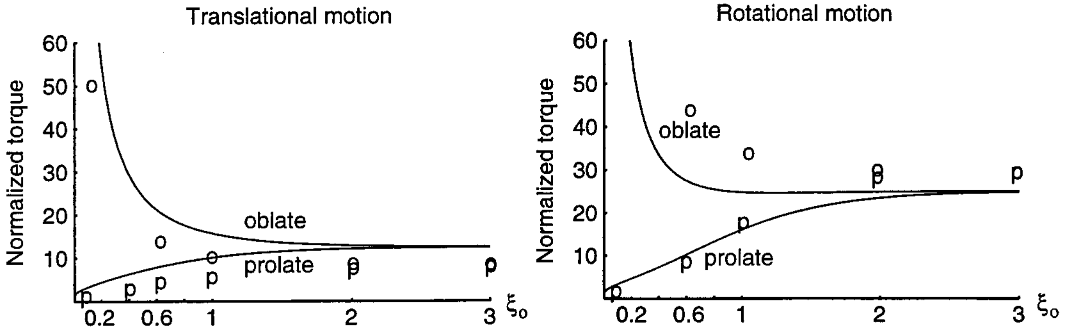

Figure 8. Left panel: The normalized, hydrodynamic torque for translational motion, $T_{tyn} = T_{ty}/(\Omega h^3)$. Right panel: The normalized, hydrodynamic torque for rotational motion, $T_{ryn} = T_{ry}/(\Omega Q)$, where $Q = h^3$ for prolate shapes and $Q = hw^2$ for oblate shapes. For both panels, *p* indicates prolate hemispheroids, *o* indicates oblate hemispheroids, and the solid lines indicate full spheroids, both oblate and prolate.

plane wall is half that of a full spheroid. This result is probably because the surface area of a hemispheroid is half that of a full spheroid and the plane wall has little effect on the hydrodynamics for thin prolate hemispheroids. As the shape becomes wider, the plane wall has more influence on the hydrodynamics along the surface of the hemispheroid, and the torque becomes larger than half that of a full spheroid.

The right panel of Figure 8 illustrates the hydrodynamic torque for rotational motion which can be obtained by taking the difference in the hydrodynamic torques for longitudinal shear and cross shear. To keep the range of values of the torque minimal we normalize by height cubed for prolate hemispheroids and by the product of height and width squared for oblate hemispheroids. We see the same trends as with translational motion, but the effect of the plane wall is more pronounced, especially for wide oblate hemispheroids. Except for very wide oblate hemispheroids, the hydrodynamic torque for the hemispheroid projecting from a plane wall is within a factor of two of that of a full spheroid with the same shape.

10. CONCLUSIONS

An indirect BEM method using spheroidal co-ordinates that efficiently and accurately compute the hydrodynamic parameters for a hemispheroid projecting from a plane wall in shear flow has been illustrated. The validity of the method was shown by applying it to a case where there is an exact solution (full spheroids in shear flow) and by comparing the results with those of a previous study for oblate hemi-spheroids. It has been shown that the hydrodynamic torque for hemispheroids projecting from plane walls has a similar shape dependence as those of full spheroids, and that for all but very wide, oblate shapes, the hydrodynamic torque for a hemispheroid projecting from a plane is within a factor of two of that of a full spheroid.

ACKNOWLEDGMENTS

The author would like to thank Professor T.F. Weiss and Professor D.M. Freeman for their insightful suggestions.

APPENDIX A. TORQUE DUE TO FLUID VELOCITY, $\Omega z\hat{\mathbf{x}}$ or $\Omega x\hat{\mathbf{z}}$

The torque due to shear on the hemispheroid can be expressed as

$$T_y = \int_S (zF_x - xF_z)\,\mathrm{d}S,$$

with F_{x_i} as

$$F_{x_i} = \mu\left(\frac{\partial U_{x_i}}{\partial x_j} + \frac{\partial U_{x_j}}{\partial x_i}\right)n_j.$$

For $U = \Omega z\hat{\mathbf{x}}$ or $U = \Omega x\hat{\mathbf{z}}$, $F_x = \mu n_z$ and $F_z = \mu n_x$. In prolate spheroidal co-ordinates, $n_z = \sinh\xi \cos\eta/\sqrt{\sinh^2\xi + \sin^2\eta}$, and $n_x = \cosh\xi \sin\eta \cos\phi/\sqrt{\sinh^2\xi + \sin^2\eta}$, and integrating around the hemispheroidal surface,

$$T_y = \int_0^{\pi/2}\int_0^{2\pi} \mathrm{d}\eta\, \mathrm{d}\phi \mu L^3 \sinh^2\xi_o \sin\eta \cosh\xi_o(\cos^2\eta - \sin^2\eta\cos^2\phi) = 0.$$

APPENDIX B. PROOF THAT THE TORQUE EXERTED BY FLUID ON A SURROUNDING SURFACE IS ZERO

We can represent the equation for Stokes flow in tensor form, i.e.

$$\frac{\partial T_{ij}}{\partial x_j} = 0, \tag{30}$$

where

$$T_{ij} = -p\delta_{ij} + \mu\left(\frac{\partial u_j}{\partial x_i} + \frac{\partial u_i}{\partial x_j}\right).$$

Using the divergence theorem and Equation (30), we can show that the force exerted by the fluid on a surrounding surface is zero, i.e.

$$F_i = \int_S T_{ij} n_j \, \mathrm{d}S = \int_V \frac{\partial T_{ij}}{\partial x_j} \, \mathrm{d}V = 0.$$

The torque exerted by the fluid on a surrounding surface can be represented as

$$T = \int_S \epsilon_{ijk} x_j T_{kl} n_l \, \mathrm{d}S, \tag{31}$$

where ϵ_{ijk} is the well-known 'completely antisymmetric tensor',

$$\epsilon_{ijk} = \begin{cases} 1 & \text{if } ijk = 123, 312, 231 \\ -1 & \text{if } ijk = 213, 132, 321 \\ 0 & \text{otherwise.} \end{cases}$$

The divergence theorem can be applied to Equation (31), so that

$$T = \int_S \epsilon_{ijk} x_j T_{kl} n_l \, \mathrm{d}S = \int_V \epsilon_{ijk} \frac{\partial}{\partial x_l} (x_j T_{kl}) \, \mathrm{d}V.$$

Since

$$\epsilon_{ijk} \frac{\partial}{\partial x_l} (x_j T_{kl}) = \epsilon_{ijk} x_j \frac{\partial T_{kl}}{\partial x_l} + \epsilon_{ijk} T_{kl} \frac{\partial x_j}{\partial x_l},$$

and

$$\epsilon_{ijk} T_{kl} \frac{\partial x_j}{\partial x_l} = 0,$$

using Equation (30), we see that the torque exerted by the fluid on a surrounding surface is zero, i.e.

$$T = \int_V \epsilon_{ijk} \frac{x_j \, \partial T_{kl}}{\partial x_l} \, \mathrm{d}V = 0.$$

APPENDIX C. THE USE OF FOURIER ANALYSIS TO DERIVE THE ϕ' DEPENDENCE OF $\mathbf{f}_{\text{fict}}(\mathbf{r}')$

$\mathbf{f}_{\text{fict}}(\mathbf{r}')$ is expressed in a Fourier series as in Equation (26). Equation (18), the pressure stokeslet, can be expressed in prolate spheroidal co-ordinates as

$$G_{px}(\xi, \eta, \phi, \xi', \eta', \phi') = \frac{(c_1(\xi, \eta)\cos\phi - c_1(\xi', \eta')(\cos\phi''\cos\phi - \sin\phi''\sin\phi))}{\sqrt{a(\xi, \eta, \xi', \eta') - b(\xi, \eta, \xi', \eta')\cos\phi''}^3}, \tag{32}$$

$$G_{py}(\xi, \eta, \phi, \xi', \eta', \phi') = \frac{(c_1(\xi, \eta)\sin\phi - c_1(\xi', \eta')(\cos\phi''\sin\phi + \sin\phi''\cos\phi))}{\sqrt{a(\xi, \eta, \xi', \eta') - b(\xi, \eta, \xi', \eta')\cos\phi''}^3}, \tag{33}$$

$$G_{pz}(\xi, \eta, \phi, \xi', \eta', \phi') = \frac{\mathrm{d}(\xi, \eta, \xi', \eta')}{\sqrt{a(\xi, \eta, \xi', \eta') - b(\xi, \eta, \xi', \eta')\cos\phi''}^3}, \tag{34}$$

where

$$\phi'' = \phi' - \phi,$$

$$a(\xi, \eta, \xi', \eta') = L^2(\cos^2\eta + \sinh^2\xi) + L'^2(\cos^2\eta' + \sinh^2\xi') - 2LL'\cos\eta\cos\eta'\cosh\xi\cosh\xi',$$

$$b(\xi, \eta, \xi', \eta') = 2LL'\sin\eta\sin\eta'\sinh\xi\sinh\xi',$$

$$c_1(\xi, \eta) = L\sinh\xi\sin\eta,$$

$$\mathrm{d}(\xi, \eta, \xi', \eta') = L\cosh\xi\cos\eta - L'\cosh\xi'\cos\eta'.$$

By substituting Equation (26) into (17), the expressions for the pressure due to impulses in the x-, y- and z-directions can be written as

$$P(\mathbf{r})|_x = \int_0^{\pi} h_1(\xi', \eta')\,\mathrm{d}\eta' \int_0^{2\pi} h_2(\xi', \eta')\,\mathrm{d}\phi' G_{px}(\xi, \eta, \phi, \xi', \eta', \phi') \times \sum_{j=0}^{\infty} (\tilde{a}_{xj}(\eta')\cos(j\phi') + \tilde{b}_{xj}(\eta')\sin(j\phi')), \tag{35}$$

$$P(\mathbf{r})|_y = \int_0^{\pi} h_1(\xi', \eta')\,\mathrm{d}\eta' \int_0^{2\pi} h_2(\xi', \eta')\,\mathrm{d}\phi' G_{py}(\xi, \eta, \phi, \xi', \eta', \phi') \times \sum_{j=0}^{\infty} (\tilde{a}_{yj}(\eta')\cos(j\phi') + \tilde{b}_{yj}(\eta')\sin(j\phi')), \tag{36}$$

$$P(\mathbf{r})|_z = \int_0^{\pi} h_1(\xi', \eta')\,\mathrm{d}\eta' \int_0^{2\pi} h_2(\xi' ,\eta')\,\mathrm{d}\phi' G_{pz}(\xi, \eta, \phi, \xi', \eta', \phi') \times \sum_{j=0}^{\infty} (\tilde{a}_{az}(\eta')\cos(j\phi') + \tilde{b}_{zj}(\eta')\sin(j\phi')), \tag{37}$$

with $G_{px}(\xi, \eta, \phi, \xi', \eta', \phi')$, $G_{py}(\xi, \eta, \phi, \xi', \eta', \phi')$ and $G_{pz}(\xi, \eta, \phi, \xi', \eta', \phi')$ given by Equations (32)–(34), and $h_1(\xi', \eta')$ and $h_2(\xi', \eta')$, the metric coefficients for prolate spheroidal co-ordinates,

$$h_1(\xi', \eta') = L'\sqrt{\sin^2\eta' + \sinh^2\xi'},$$

$$h_2(\xi', \eta') = L'\sin\eta'\sinh\xi'.$$

With $\phi' = \phi'' + \phi$, $\cos \phi' = \cos \phi'' \cos \phi - \sin \phi'' \sin \phi$, and $\sin \phi' = \sin \phi'' \cos \phi + \cos \phi'' \sin \phi$, Equations (35)–(37) can be expressed as

$$\begin{aligned}
P(\mathbf{r})|_x = {} & \int_0^{\pi} h_1(\xi', \eta')\,\mathrm{d}\eta' \int_0^{2\pi} h_2(\xi', \eta')\,\mathrm{d}\phi'' G_{px}(\xi, \eta, \phi, \xi', \eta', \phi') \\
& \times \sum_{j=0}^{\infty} (\tilde{a}_{xj}(\eta')(\cos j\phi'' \cos j\phi - \sin j\phi'' \sin j\phi) \\
& + \tilde{b}_{xj}(\eta')(\sin j\phi'' \cos j\phi + \cos j\phi'' \sin j\phi)), \\
P(\mathbf{r})|_y = {} & \int_0^{\pi} h_1(\xi', \eta')\,\mathrm{d}\eta' \int_0^{2\pi} h_2(\xi', \eta')\,\mathrm{d}\phi'' G_{py}(\xi, \eta, \phi, \xi', \eta', \phi') \\
& \times \sum_{j=0}^{\infty} (\tilde{a}_{yj}(\eta')(\cos j\phi'' \cos j\phi - \sin j\phi'' \sin j\phi) \\
& + \tilde{b}_{yj}(\eta')(\sin j\phi'' \cos j\phi + \cos j\phi'' \sin j\phi)), \\
P(\mathbf{r})|_z = {} & \int_0^{\pi} h_1(\xi', \eta')\,\mathrm{d}\eta' \int_0^{2\pi} h_2(\xi', \eta')\,\mathrm{d}\phi'' G_{pz}(\xi, \eta, \phi, \xi', \eta', \phi') \\
& \times \sum_{j=0}^{\infty} (\tilde{a}_{zj}(\eta')(\cos j\phi'' \cos j\phi - \sin j\phi'' \sin j\phi) \\
& + \tilde{b}_{zj}(\eta')(\sin j\phi'' \cos j\phi + \cos j\phi'' \sin j\phi)),
\end{aligned}$$

Since ϕ' is integrated over a full period of 2π, the integration can equally be performed over a full period in ϕ''.

By substituting Equations (32)–(34) into the above expressions for $P_x(\mathbf{r})$, $P_y(\mathbf{r})$ and $P_z(\mathbf{r})$ and performing the integrations over a full period of ϕ'', we can determine which terms will give only a $\cos \phi$ dependence. Note that odd functions of ϕ'' integrate to zero. One possible term is the $\tilde{a}_{x0}(\eta')$ term. Two other possible terms are $\tilde{a}_{x2}(\eta') \cos 2\phi'$ and $\tilde{b}_{y2}(\eta') \sin 2\phi'$ if $\tilde{a}_{x2}(\eta') = \tilde{b}_{y2}(\eta')$. The only other term possible is $\tilde{a}_{z1}(\eta') \cos \phi'$. Therefore, $\mathbf{f}_{\text{fict}}(\eta', \phi')$ can be expressed as

$$f_{\text{fict},x}(\eta', \phi') = \tilde{a}_{x0}(\eta') + \tilde{a}_{x2}(\eta') \cos 2\phi', \tag{38}$$

$$f_{\text{fict},y}(\eta', \phi') = \tilde{a}_{x2}(\eta') \sin 2\phi', \tag{39}$$

$$f_{\text{fict},z}(\eta', \phi') = \tilde{a}_{z1}(\eta') \cos \phi'. \tag{40}$$

Equations (38)–(40) are consistent with those found in References [7] (S. Haber, personal communication), and also give the correct ϕ dependence of the velocities expressed in Equations (23)–(25).

To facilitate the analytic integration in ϕ', we will use equivalent representations of Equations (38)–(40), given in Equations (27)–(29).

APPENDIX D. ANALYTIC SOLUTIONS

The analytic solutions are derived from Reference [14]. For the full spheroid with surface velocity equal to $\Omega z \hat{\mathbf{x}}$, the velocity is expressed as

$$\mathbf{U}(\mathbf{r}) = \alpha_2 x[(2A_1 + A_3)\hat{\mathbf{z}} + 2(x\hat{\mathbf{x}} + y\hat{\mathbf{y}})B_{3,1}] + \gamma_2[2\hat{\mathbf{x}}B_{1,1} - \hat{\mathbf{z}}xA_3] + 4\beta_2\nabla[x(L^2B_{3,1} - B_{3,3})],$$

with $e = 1/\cosh\xi_o$ and $L_e = \log(1 + e/1 - e)$.

The function $B_{m,n}(x, y, z)$ is defined as

$$B_{1,0} = \log\frac{R_2 - (z - L)}{R_1 - (z + L)}, \qquad B_{1,1} = R_2 - R_1 + zB_{1,0},$$

$$B_{3,0} = \frac{1}{r^2}\left(\frac{z + L}{R_1} - \frac{z - L}{R_2}\right), \qquad B_{3,1} = \left(\frac{1}{R_1} - \frac{1}{R_2}\right) + zB_{3,0},$$

$$B_{m,n} = -\frac{L^{n-1}}{m-2}\left(\frac{1}{R_2^{m-2}}, + \frac{(-1)^n}{R_1^{m-2}}\right) + \frac{n-1}{m-2}B_{m-2,n-2} + zB_{m,n-1} \quad \text{for} \quad n \geq 2,$$

and

$$A_1 = zB_{3,1} - B_{3,2}, \qquad A_3 = L^2B_{3,0} - B_{3,2},$$

$$\gamma_2 = \Omega[-2e + (1 + e^2)L_e]^{-1},$$

$$\alpha_2 = e^2\gamma_2[-2e + (1 - e^2)L_e][2e(2e^2 - 3) + 3(1 - e^2)L_e]^{-1},$$

$$\beta_2 = \alpha_2(1 - e^2)/(4e^2).$$

The pressure is expressed as

$$P(\mathbf{r}) = \alpha_2\int_{-L}^{L}\frac{2(L^2 - z'^2)3x(z - z')}{\sqrt{x^2 + y^2 + (z - z')^{25}}}\,\mathrm{d}z'.$$

The torque for this case is described by

$$T = \frac{-32}{3}\pi\mu L^3\gamma_2\hat{\mathbf{y}}.$$

For the full spheroid with surface velocity equal to $-\Omega x\hat{\mathbf{z}}$, the velocity is expressed as

$$\mathbf{U}(\mathbf{r}) = \alpha_3 x[(2A_1 + A_3)\hat{\mathbf{z}} + 2(x\hat{\mathbf{x}} + y\hat{\mathbf{y}})B_{3,1}] + \gamma_3[2\hat{\mathbf{x}}B_{1,1} - \hat{\mathbf{z}}xA_3] + 4\beta_2\nabla[x(L^2B_{3,1} - B_{3,3})],$$

with

$$\gamma_3 = \Omega(1 - e^2)[-2e + (1 + e^2)L_e]^{-1},$$

$$\alpha_3 = 2e^2\gamma_3[-2e + L_e][2e(2e^2 - 3) + 3(1 - e^2)L_e]^{-1},$$

$$\beta_3 = \alpha_3(1 - e^2)/(4e^2).$$

The pressure is expressed as

$$P(\mathbf{r}) = \alpha_3\int_{-L}^{L}\frac{2(L^2 - z'^2)3x(z - z')}{\sqrt{x^2 + y^2 + (z - z')^{25}}}\,\mathrm{d}z'.$$

The torque for this case is described by

$$T = \frac{-32}{3}\pi\mu L^3\gamma_3\hat{\mathbf{y}}.$$

The exact solutions for oblate spheroids can be derived from the solutions for prolate spheroids by letting $\cosh\xi_o \to j\sinh\xi_o$, and $L \to -jL$.

REFERENCES

1. W.R. Dean, 'Note on the slow motion of fluid', *Proc. Camb. Phil. Soc.*, **32**, 598–613 (1936).
2. A.M.J. Davis and M.E. O'Neill, 'Separation on a slow linear shear flow past a cylinder and a plane', *J. Fluid Mech.*, **81**, 551–564 (1977).
3. D.M. Freeman and T.F. Weiss, 'Hydrodynamic analysis of a two-dimensional model for micromechanical resonance of free-standing hair bundles', *Hear. Res.*, **48**, 37–68 (1990).
4. M.E. O'Neill, A sphere in contact with a plane wall in a slow linear shear flow', *Chem. Eng. Sci.*, **23**, 1293–1298 (1968).
5. W.A. Hyman, 'Shear flow over a protrusion from a plane wall', *J. Biomech.*, **5**, 45–48, Corrigendam on page 643, 1972.
6. T.C. Price, 'Slow linear shear flow past a hemispheroidal bump in a plane wall', *Q. J. Mech. Appl. Math.*, **38**, 93–104 (1985).
7. C. Pozrikidis, 'Shear flow over a protuberance on a plane wall', *J. Eng. Math.*, **31**, 29–42 (1997).
8. W.S.J. Uijttewaal, E. Nijhof and R. M. Heethaar, 'Droplet migration, deformation, and orientation in the presence of a plane wall: A numerical study compared with analytic theories', *Phys. Fluids A*, **5**, 819–825 (1992).
9. T.M. Fischer, 'A boundary integral method for the numerical computation of the forces exerted on a sphere in viscous incompressible flows near a plane wall', *J. Appl. Math. Phys.*, **38**, 339–365 (1987).
10. C. Pozrikidis, 'Shear flow over a plane wall with an axisymmetric cavity or a circular orifice of finite thickness', *Phys. Fluids*, **6**, 68–79 (1994).
11. H. Lamb, *Hydrodynamics*, 6th edn, Dover Publications, New York, 1945.
12. P. Moon and D.E. Spencer, *Field Theory Handbook*, 2nd edn, Springer, Berlin, 1971.
13. J.R. Blake, 'A note on the image system for a stokeslet in a no-slip boundary', *Proc. Camb. Phil. Soc.*, **70**, 303–310 (1971).
14. A.T. Chwang and T.Y. Wu, 'Hydromechanics of low-Reynolds-number flow, Part 2. Singularity method for Stokes flows, *J. Fluid Mech.*, **67**, 787–815 (1975).
15. A.A. Becker, *The Boundary Element Method in Engineering—A Complete Course*, 1st edn, McGraw-Hill, London, 1992.
16. C. Pozrikidis, 'A study of linearized oscillatory flow past particles by the boundary integral method', *J. Fluid Mech.*, **202**, 17–41 (1989).
17. C. Pozrikidis, 'Boundary integral and singularity methods for linearized viscous flow', Cambridge University Press, Cambridge, UK, 1992.
18. W.R. Dean and M.E. O'Neill, 'A slow motion of viscous liquid caused by the rotation of a solid sphere', *Mathematika*, **10**, 13–24 (1963).
19. Steven Wolfrem, Mathematica 2.0. Wolfrem Research, Champaign, Ill., 1991.